JOURNAL OF CATALYSIS 149, 81–91 (1994)

Acetone Oxidation in a Photocatalytic Monolith Reactor

Michael L. Sauer and David F. Ollis

Department of Chemical Engineering, North Carolina State University, Raleigh, North Carolina 27695-7905

Received November 19, 1993; revised May 23, 1994

Photocatalyzed oxidation of acetone (70–400 mg/m^3) in air was carried out using near-UV illuminated TiO_2 (anatase) coated on the surface of a ceramic honeycomb monolith. Considerable adsorption of acetone and water was noted on the catalyst coated monolith; these uptakes were described with a Langmuir adsorption isotherm for acetone and a modified BET adsorption isotherm for water. The acetone photocatalyzed disappearance kinetics on the TiO_2 were determined with initial rate differential conversion, recycle reactor data and were analyzed using a Langmuir–Hinshelwood rate form coupled with a reactant mass balance including appreciable acetone monolith adsorption. The model, with parameters evaluated from initial rate data, is then shown to satisfactorily predict reactor behavior at all conversions. These kinetics and design results, together with earlier literature for photocatalytic oxidation of alkanes, 1-butanol, toluene, trichloroethylene, and odor compounds, indicate a potential for use of the photocatalytic monolith configuration for removal of all major classes of air contaminants.

1. INTRODUCTION

The oxidative removal of trace contaminants from air is a growing research area (1–9). Heterogeneous photocatalysis has been shown in recent years to oxidize a broad contaminant range; potential air treatment applications arise in building environments, space craft, factories, and homes. Attractive advantages with photocatalysis for air treatment and purification are ambient temperature and pressure operation (1), use of molecular oxygen as the oxidant (1), and final oxidation products that are usually innocuous (1) (CO_2 and H_2O for the oxidation of small hydrocarbons).

Photocatalysis utilizes a greater-than-band-gap excitation source, UV or near-UV light for TiO_2 ($\geq$350 nm) (1), to excite electrons from the valence band into the conduction band of the semiconductor oxide. The photoproduced holes and electrons can then either recombine (nonproductive) or migrate individually to the catalyst surface where they may participate in useful redox reactions with adsorbed species. For example, a surface hole may react with an adsorbed hydroxyl group to produce a strong oxidant, the hydroxyl radical, which in turn oxidizes an adsorbed contaminant to yield a photocatalysis oxidation product. Alternately, a hole may directly oxidize an adsorbed contaminant (fragment). Adsorbed oxygen species derived from molecular oxygen may combine with conduction band photoexcited electrons, thereby "scavenging" electrons and preventing the undesired recombination of holes and electrons.

Earlier work by the automobile industry utilized a honeycomb monolith configuration on a large scale for thermal catalytic converters (10). Central advantages of the monolith configuration are a low pressure drop and a high surface-area-to-volume ratio (10, 11); the low pressure drop allows the force of the exhaust gases from the engine to drive the gas flow through the catalytic reactor with a negligible engine back pressure. The relationship between the flowrate and pressure drop across a monolith follows the Poiseuille equation (10). A disadvantage of thermal catalytic converter technology is the need for high temperature operation, 400–800°F (12), to maintain high conversion rates. These temperatures are impractical for treatment of trace contaminants in ambient temperature air. The use of a photocatalytic monolith for trace contaminant oxidative removal allows retention of the low pressure drop characteristic of the monolith coupled with the room temperature, low pressure photodestruction of the pollutants.

Gas–solid heterogeneous photocatalytic oxidation has been demonstrated for alkanes (2), aromatics (toluene (3, 7), *m*-xylene (4), a halocarbon (trichloroethylene) (5, 6, 8), an alcohol (1-butanol) (4), an aldehyde (formaldehyde) (4), and a ketone (acetone) (4, 9). Our prior acetone study (4) showed that acetone photooxidation followed a Langmuir–Hinshelwood kinetic analysis and did not proceed through any kinetically significant intermediates.

For photocatalyst commercial application, the influence of relative humidity should be routinely studied since (i) most contaminated air streams are also (partially) humidified, containing $\approx$1–2% water vapor, and (ii) the influence of such 10,000–20,000 ppm H_2O on the conversion kinetics of 1–1000 ppm contaminant can be strong and is reactant specific: these H_2O levels enhance toluene conversion rates (3), inhibit acetone (4) and TCE (5, 6) conver-

0021-9517/94 $6.00

sion, and can activate (low humidity) or inhibit (high humidity) *m*-xylene conversion (4).

Suzuki *et al.* (Toyota R/D) studied photooxidation of trace odor compounds in air over TiO_2 in the first report of a photocatalytic monolith recirculating batch reactor (7). Acetaldehyde, isobutyric acid, toluene, methylmercaptan, hydrogen sulfide, and trimethylamine were individually converted; disappearance kinetics were analyzed with a pseudo-first-order equation.

The present gas–solid photocatalytic monolith reactor study was undertaken for two reasons:

(i) The study by Suzuki *et al.* (7) was limited to odor compounds in low concentrations (5–80 ppm). The present work was undertaken to show that the monolith configuration can treat single and multiple contaminated air feed streams that contain higher contaminant concentrations of interest in building and spacecraft air treatment up to 400 mg/m^3, and to include the influence of relative humidity on reaction kinetics.

(ii) Suzuki *et al.* (7) reported pseudo-first-order rate constants describing batch photooxidation kinetics. In the present study, we show that such a batch recycle system requires a comprehensive analysis including reactor dynamics, reactant physical adsorption on the catalyst coated monolith, and photooxidation kinetics. This treatment is shown here to give an accurate predictive description of the recirculating, batch system behavior. Inclusion of the adsorbed acetone inventory provides a catalytic rate constant several times larger than that estimated by Suzuki.

2. METHOD

Our reactor system (Fig. 1) incorporates a ceramic honeycomb monolith having titanium dioxide particles coated on its surface. The gas-tight recirculating loop is constructed of 3-in.-ID glass sections and couplings (Ace Glass). In differential conversion operation, the recycle loop acts as a continuous stirred tank (CST), maintaining a well mixed gas volume from which GC samples are taken. The monolith is treated as a CSTR since the conversion per pass was ≤0.22% for all runs.

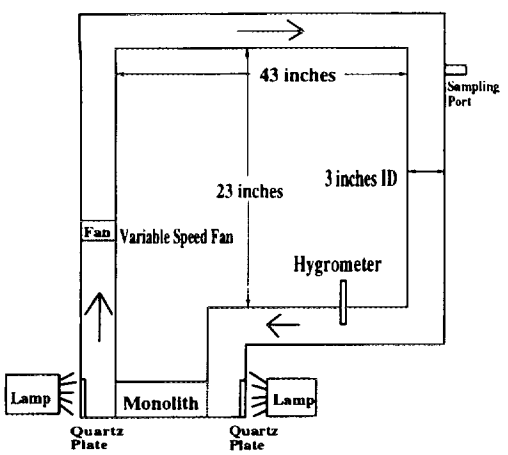

FIG. 1. Experimental photocatalytic monolith reactor system.

The reactor configuration shown provides illumination of the monolith channels from light sources located outside of the system. Quartz plate windows allow use of UV light if desired. The experimental apparatus utilized two 100-W UV medium pressure mercury lamps with a near-UV filter attachment, with one lamp located at each end of the monolith. Recirculation air flow in the system is driven by a 3-in.-diameter, 24-V DC fan, which provides a maximum recirculation rate of 3.3 CFM, corresponding to a system recirculation time of 11.8 sec and a residence time per pass in the monolith of 0.45 sec (space velocity = 304 hr^{-1}). The gas sampling point in the recycle loop allows periodic monitoring of reactant and product concentrations. All air samples were analyzed by gas chromatography (Perkin–Elmer Sigma Series 1) operating with a flame ionization detector (FID) and SS Alltech column with AT-1000 (1%) on 60/80 Graphac GB packaging. A hygrometer equipped with a thermocouple was added to the system to measure simultaneously the relative humidity and temperature, from which the gas-phase water concentration may be calculated. Finally, a pressure gauge, vacuum port, gas tank inlet feed, and flowrate calibration ports were installed to allow monitoring and safe use of the system.

The catalyst powder used was Degussa P25 titanium dioxide, which is mostly anatase with a primary particle diameter of 30 nm and a specific surface area of 50 ± 15 m^2/gm (Degussa). The P25 particles were spherical and nonporous, with a stated purity of >99.5% TiO_2 (Degussa). Stated impurities include Al_2O_3 (<0.3%), HCl (<0.3%), SiO_2 (<0.2%), and Fe_2O_3 (<0.01%). The ceramic honeycomb monoliths were obtained from Corning, shaped into 3-in.-diameter, 6-in.-long cylinders, then coated with untreated titanium dioxide powder. The cordierite monoliths had a roughly uniform pore size of about 10 μm and a BET surface area of ≤0.4 m^2/gm (Corning), which for our 325.9-g monolith gave ≤130 m^2 of internal pore surface area. The monolith used here has square channels of width 0.167 in. (Corning), with a total apparent external surface area of 3550 cm^2 for all channels in the 3-in.-diameter monolith.

The coating of TiO_2 particles on the monolith support was accomplished by dipping the monolith into a well mixed water slurry of 5 wt% TiO_2 in deionized water for about 15 sec. The coated monolith was dried in air at 105°C for 3–4 hr to remove bulk water, leaving a layer of TiO_2 particles on the monolith surface. This coating process was repeated 11 times, resulting in deposition of

13.80 g of TiO_2 possessing a coated catalyst surface area of 690 m^2. The approximate thickness of the TiO_2 film was at least 10.1 μm, calculated by assuming a nonporous, uniform deposition of crystalline anatase TiO_2 (3.84 gm^3/cm). Teichner *et al.* have shown that 99% of light absorption occurred within a 4.5-μm powder layer of TiO_2 (1). Our coating process produced a powder film well above the minimum thickness required for total light absorption by the monolith channel wall.

In a typical experiment, the air recirculation is established. Next, the desired amount of liquid water is injected and allowed to evaporate (aided by a heat gun), circulate, and come to adsorption equilibrium with the (coated) monolith. The desired amount of acetone (HPLC grade) is then injected as liquid and allowed to evaporate, circulate, and also reach gas–solid equilibration. The lamps outside the system are turned on to warm up, with care taken to not yet illuminate the catalyst. When a steady-state acetone gas-phase concentration is reached within the recirculating system, the catalyst is illuminated, and the gas phase is sampled periodically to provide acetone concentration vs time data, from which the total rate of disappearance of acetone due to photocatalytic reaction can be calculated under various assumptions. Samples are taken every 10–30 min, depending upon the total expected length of the run.

3. RESULTS

We expected the large internal pore surface area of the honeycomb monolith (130 m^2) and TiO_2 catalyst (690 m^2) to lead to significant physical adsorption of water and acetone. The results of the present study therefore include: (i) measurement and model of the water adsorption isotherm, (ii) measurement and model of the acetone and water combined adsorption isotherm, (iii) measurement of acetone photooxidation kinetics and an initial rate kinetic analysis to determine the photocatalytic model parameters (reaction rate and binding constants), and (iv) model of the recycle system transient behavior including high conversions of interest in air treatment and comparison of predictive model and experiment.

3.1. Water Adsorption

The water isotherm was measured separately on a catalyst-coated and an uncoated monolith. The water isotherm for the catalyst layer was calculated by taking the difference between the adsorption on the catalyst-coated and uncoated monoliths. The water isotherms were determined by adding a known amount of water, measuring the relative humidity and temperature in the equilibrated gas–solid system, calculating the gas-phase water concentration, then using a water mass balance to determine the amount of adsorbed water. The experimental data was obtained over the range 0–75% relative humidity at 80°F, which is near the human comfort range in a building environment (20–60% relative humidity, 72–78°F) (13).

3.1.1. Uncoated monolith. The measured fractional surface coverage of water versus measured gas-phase water concentration for the uncoated monolith at 80°F appears in Fig. 2. These data exhibit the shape of a type-II adsorption isotherm (14), which indicates that multilayer adsorption is occurring. The experimental adsorption data was therefore modeled using a modified BET equation (14),

$$\Theta_w^{mon} = \frac{M_w^{ads}}{\mu_{mon}} = \left(\frac{K_B^{mon} f(T) V_g C_w}{1 - f(T) V_g C_w}\right) \left(\frac{1 - (n+1)(f(T)V_gC_w)^n + n(f(T)V_gC_w)^{n+1}}{1 + (K_B^{mon} - 1) f(T) V_g C_w - K_B^{mon} (f(T)V_gC_w)^{n+1}}\right), \quad [1]$$

where Θ_w^{mon} is the surface adsorption coverage of water (dimensionless); M_w^{ads} is the mass of water adsorbed on the monolith (mg); C_w is the water gas-phase concentration (mg/m^3); K_B^{mon} is the water adsorption constant (dimensionless); μ_m^{mon} is the maximum number of water molecules in a monolayer (mg); n is the maximum number of layers of adsorption occurring (layers); V_g is the system gas-phase volume (m^2); and

$$f(T) = 1.881x\,10^{-4} T(K)/\exp\left(\frac{18.6719T(°F) + 45.077}{T(°F) + 391.0}\right) \quad (mg^{-1}).$$

The Eq. [1] parameter μ_{mon} was calculated from the monolith surface area, assuming an adsorption cross sec-

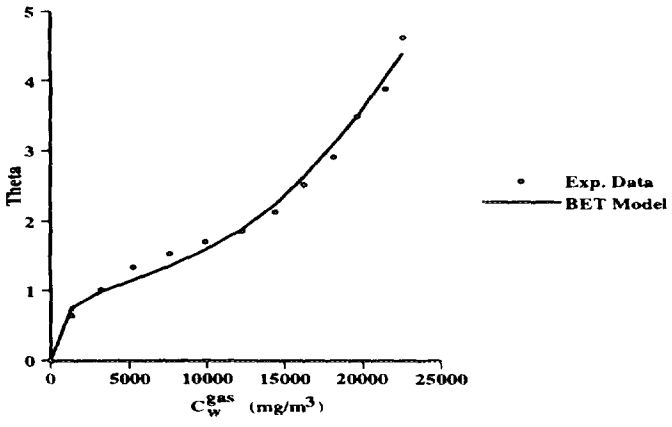

FIG. 2. Physical adsorption experimental data and model fit for water on the uncoated monolith using a BET equation at 80°F.

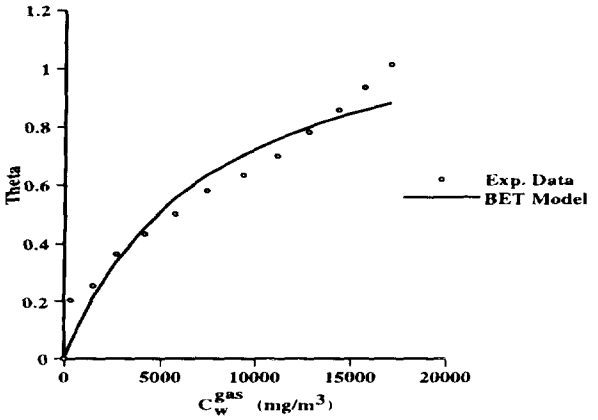

FIG. 3. Physical adsorption experimental data and model fit for water on the TiO_2 catalyst using a single BET equation at 80°F.

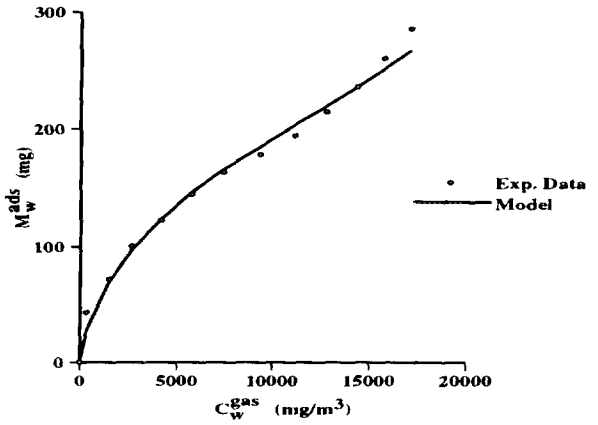

FIG. 4. Physical adsorption experimental data and model fit for water on the coated monolith using two BET equations at 80°F.

tional area of 11.7 Å^2/water molecule (estimated from the density of liquid water). The parameters K_B^{mon} and n were then varied to give the best fit of the experimental data (Fig. 2). The resulting parameter values are n = 9.4 layers, μ_m = 40.0 mg, K_B^{mon} = 43.0 (dimensionless), and R^2 = 0.989.

The best fit criteria was determined by maximizing the nonlinear regression parameter R^2 over all the experimental data:

$$R^2 = 1 - \left(\frac{\Sigma(\Theta_w^{exp} - \Theta_w^{calc})^2}{\Sigma(\Theta_w^{exp} - \Theta_w^{avg})^2}\right). \quad [2]$$

3.1.2. TiO_2 catalyst layer. The experimental data for fractional surface coverage of water vs gas-phase water concentration for the TiO_2 catalyst layer at 80°F appears in Fig. 3 compared to a fitted modified BET equation (Eq. [1]). The resulting parameter values are n = 1.3 layers, μ_m = 176.3 mg, K_B^{mon} = 4.2 (dimensionless), and R^2 = 0.943.

3.1.3. Coated monolith. The coated monolith data was modeled by adding together the individual modified BET equations for the uncoated monolith (Fig. 2) and the TiO_2 catalyst (Fig. 3). Figure 4 compares the resulting model to the experimental data at 80°F for the coated monolith in a plot of mass of water adsorbed vs gas-phase water concentration (R^2 = 0.990).

The coated monolith experimental water adsorption data can also fit a single modified BET equation (Fig. 5), with resulting parameter values n = 5.8 layers, μ_m = 118.4 mg, and K_B^{mon} = 28.8 (dimensionless).

3.1.4. Effect of acetone. Next, the effect of increasing gas-phase acetone on water adsorption was measured and seen to be negligible.

3.2. Acetone Adsorption

The acetone adsorption isotherm was measured on the coated monolith; it was expected to be a function of both acetone and water gas-phase concentration and of temperature. Each acetone isotherm was measured at 80°F with a fixed total amount of water in the system over a range of 0–25 μl total acetone in the system. The total water amounts used were 0, 200, 400, and 600 mg. The adsorption data (Fig. 6) show that at a constant acetone gas-phase pressure, the mass of acetone adsorbed on the coated monolith decreases as the total mass of water in the system increases; acetone physical adsorption never reaches monolayer coverage.

The acetone physical adsorption inventory on the coated monolith was modeled using a single nondissociative Langmuir isotherm,

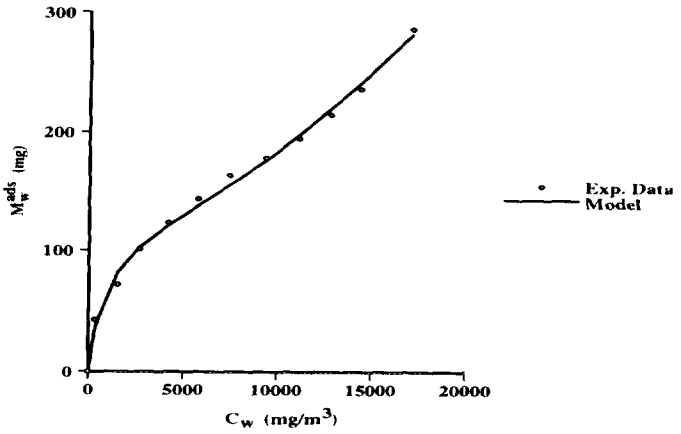

FIG. 5. Physical adsorption model fit for water on the coated monolith using a single BET equation at 80°F.

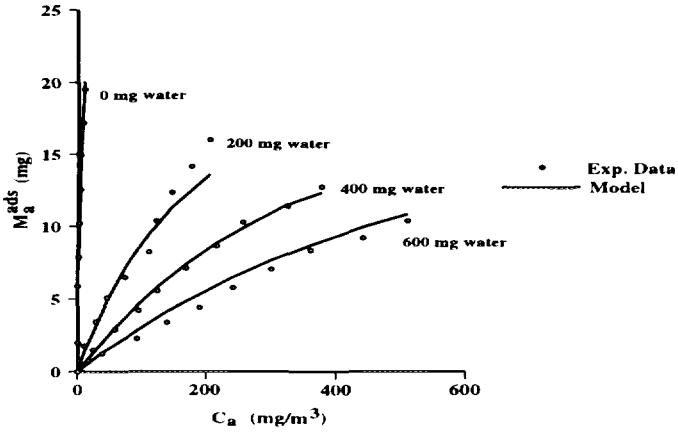

FIG. 6. Physical adsorption experimental data and model fit for acetone on the coated monolith using a Langmuir equation in the presence of varying amounts of water at 80°F.

$$\Theta_A^{overall} = \frac{M_A^{ads}}{\mu_A^{overall}} = \frac{K_A^{overall} C_A}{1 + K_A^{overall} C_A + K_w^{overall} C_w}, \quad [3]$$

where $\Theta_A^{overall}$ is the surface adsorption coverge of acetone (dimensionless); M_A^{ads} is the mass of acetone adsorbed on the monolith (mg); C_A is the acetone gas-phase concentration (mg/m^3); C_w is the water gas-phase concentration (mg/m^3); $K_A^{overall}$ is the acetone binding constant (m^3/mg); $K_w^{overall}$ is the water binding constant (m^3/mg); and $\mu_A^{overall}$ = is the maximum number of acetone molecules in a monolayer (mg).

The constants $\mu_A^{overall}$, $K_A^{overall}$, and $K_w^{overall}$ were fit to the experimental data and R^2 (Equ. [2]) was maximized (as before) to obtain the "best fit." The resulting parameters were $\mu_A^{overall}$ = 28.2 mg; $K_A^{overall}$ = 0.208 m^3/mg; $K_w^{overall}$ = 0.0102 m^3/mg, and R^2 = 0.975.

Figure 6 shows the resulting model fit compared to the experimental data. These results are used later in our kinetic model, as the acetone disappearance rate must include both decreased gas-phase and adsorbed phase(s) contributions.

3.3. *Acetone Photooxidation*

The measured water and acetone isotherms are now used in the acetone photooxidation kinetic analysis, which involves the determination of kinetic parameters and the development of a transient model to predict the system behavior. The assumption is made that there are no kinetically significant intermediates or products, and that only acetone and water are adsorbed on the surfaces. Carbon dioxide adsorption was not measured, but was assumed to be negligible. Thus, the acetone photocatalytic destruction on the TiO_2 monolith follows a simple Langmuir–Hinshelwood rate form, as found earlier for the same TiO_2 samples used in a powder layer (4),

$$-r_A = \frac{kKC_A}{1 + KC_A}, \quad [4]$$

where k is the acetone reaction rate constant; K is the binding constant; C_g is the acetone gas phase concentration; and r_A is the acetone reaction rate per volume of active (illuminated) catalyst.

Equation [4] is only applicable for a fixed water level and would yield a different reaction rate constant (k) at a different water level due to the inhibition of acetone photooxidation by water (4).

In the absence of significant adsorption on the coated monolith, and assuming a uniform gas-phase concentration throughout the monolith,

$$-V_c^{act} r_A = -V_g \frac{dC_A}{dt}, \quad [5]$$

where V_g is the gas volume of the monolith reactor system and V_c^{act} is the active catalyst volume.
Combining Eqs. [4] and [5],

$$\frac{kKC_A}{1 + KC_A} = \frac{-V_g}{V_c^{act}} \frac{dC_A}{dt}. \quad [6]$$

Equation [6] does not, however, include acetone physical adsorption/desorption from the coated monolith. Over the acetone concentrations used (70–400 mg/m^3 initial concentration) and for a total fixed water content of 400 mg (≈11,000 mg/m^3, 40% Relative Humidity) at 80°F, 64–77% of the total acetone injected was initially adsorbed on the coated monolith. Kinetic rate evaluation for acetone must account for the change over time in mass of acetone reversibly adsorbed on the coated monolith as well as in the gas phase. A full transient mass balance on acetone in the system yields

$$-(-r_A)V_c^{act} = V_g \frac{dC_A}{dt} + \frac{dM_A^{ads}}{dt}, \quad [7]$$

where M_A^{ads} is given by Eq. [3]. Combining Equations [3], [4], and [7] gives

$$-\frac{kKC_A V_c^{act}}{1 + KC_A} = d\left(V_g C_A + \frac{\mu_A K_A C_A}{1 + K_A C_A + K_w C_w}\right) \Big/ dt, \quad [8]$$

which can be simplified to

$$-\frac{kKC_g V_c^{act}}{1 + KC_A} = \frac{d\Psi}{dt}, \quad [9]$$

where we define the variable Ψ (total acetone mass) as

$$\Psi \equiv V_g C_A + \frac{\mu_A K_A C_A}{1 + K_A C_A + K_w C_w}. \quad [10]$$

Rearranging Equation [9],

$$\frac{-1}{d\Psi/dt} = \frac{1}{kKV_c^{act} C_A} + \frac{1}{kV_c^{act}}. \quad [11]$$

The variable Ψ in Eqs. [9], [10], and [11] represents the total mass of acetone, which is changing continuously over time. Experiments were performed with total acetone amounts of 5, 10, 15, 20, and 25 μl (70 – 400 mg/m^3), a total water content of 400 mg (≈11,000 mg/m^3), and a constant temperature of 80°F. The maximum per pass conversion for any of the experimental runs was calculated to be ≈0.22%, which justifies the differential conversion assumption made previously.

The experimental results for these five runs are shown collectively in Fig. 7. A plot of the initial rate data as $-1/(d\Psi/dt)_{|t=0}$ vs $1/C_{A|_{t=0}}$ can be represented by a straight line (Fig. 8), with a linear least squares fit (solid line, Fig. 8) having a slope of 1168 min/m^3 and an intercept of 12.50 min/mg. From the model, the slope and intercept are given by

$$\text{slope} = \frac{1}{kKV_c^{act}} \quad [12]$$

and

$$\text{intercept} = \frac{1}{kV_c^{act}}. \quad [13]$$

The value of V_c^{act} was determined to be 0.20 cm^3 (see the Appendix), while V_g was calculated to be 18420 cm^3.

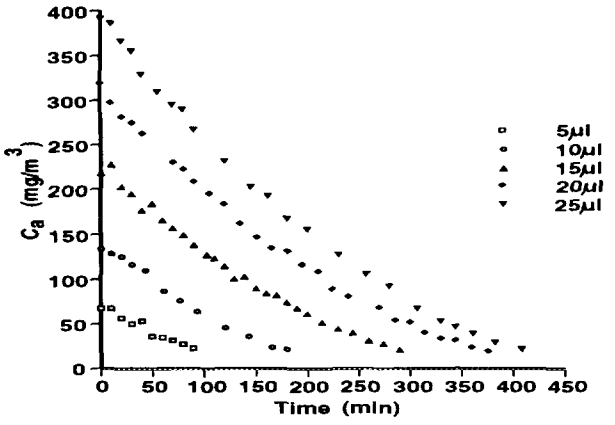

FIG. 7. Acetone photooxidation experimental data at (T = 80°F) for 5, 10, 15, 20, and 25 μl total of initial liquid acetone in the system (70 – 400 mg/m^3).

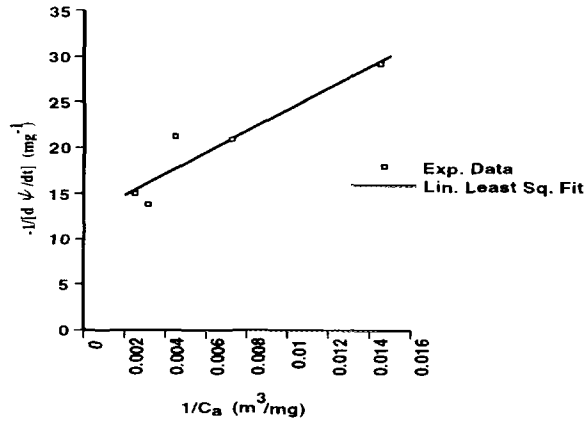

FIG. 8. Determination of acetone initial rate kinetic parameters.

Given V_c^{act} and V_g, the resultant values for k and K (with 400 mg total water) are

$$k = 0.40 \frac{\text{mg}}{\text{cm}^3\text{cat} - \text{min}} \quad [14]$$

and

$$\text{K} = 0.0107 \frac{\text{m}^3}{\text{mg}}. \quad [15]$$

The importance of including acetone adsorption on the coated monolith is checked by calculating the initial reaction rates of acetone for three different cases: (i) coated monolith adsorption is neglected, (ii) gas-phase acetone mass is neglected, and (iii) coated monolith adsorption and gas-phase acetone mass included. The initial rate equations for these three cases are:

Case 1 (coated monolith adsorption is negligible),

$$-(-r_{A_{|t=0}}) = \frac{V_g}{V_c^{act}} \left(\frac{dC_A}{dt}\right)_{|t=0}; \quad [16]$$

Case 2 (gas mass changes are neglected),

$$-(-r_{A_{|t=0}}) = \frac{1}{V_c^{act}} \left(\frac{dM_A^{ads}}{dt}\right)_{|t=0}$$

$$= \frac{1}{V_c^{act}} \left(d\left(\frac{(28.2)(0.208)C_A}{1 + 0.208C_A + 0.0102C_w}\right) \Big/ dt\right)_{|t=0}; \quad [17]$$

Case 3 (coated monolith adsorption and gas mass changes both included),

TABLE 1

Calculated Initial Rate Data with and without Inclusion of Monolith Adsorption (400 mg Water) (Rxn Rate Units: $-r_A \Rightarrow$ gm/(m^3_{cat} − min))

$V^{tot}_{acet.}$ (μl)	$(C_A)_{t=0}$ (mg/m^3)	Rxn rate (no ads.)	Rxn rate (ads. only)	Rxn rate (combined)	% Rxn rate (gas phase)
5	61.0	18.5	41.2	59.7	31.0
10	131.8	26.8	56.0	82.8	32.4
15	213.6	31.9	48.8	80.7	39.5
20	307.3	52.4	71.1	123.5	42.4
25	413.5	51.7	61.1	112.8	45.8

$$-(-r_{A_{t=0}}) = \frac{V_g}{V_c^{act}}\left(\frac{dC_A}{dt}\right)_{|t=0} + \frac{1}{V_c^{act}}\left(d\left(\frac{(28.2)(0.208)C_A}{1 + 0.208C_A + 0.0102C_w}\right) \Big/ dt\right)_{|t=0}. \quad [18]$$

Table 1 lists the results of the initial rate calculations for the acetone concentrations used in the experimental runs. The importance of the coated monolith adsorption is apparent from these results, which show that neglecting the coated monolith adsorption will lead to a large underprediction (55–70%) of the actual rate of reaction. We note that this adsorbed transient inventory of reactant must be included in batch (recycle) reactor analyses of the kind often used in heterogeneous photocatalysis. For steady-state flow reactors, at lab or commercial scale, the adsorbed inventory is constant, and does not contribute to reaction rate analysis.

3.4. Acetone Transient Model

Figure 9 shows the configuration that was assumed for the model calculations. The system assumed is a CSTR (monolith section) in series with a CST (system recirculating loop), where q is the volumetric flowrate; C_i is the concentration of acetone in CST (C_S) or CSTR (C_R); V_i is the volume of CST (V_S) or CSTR (V_R); V_g is the combined gas volumes of the CST and CSTR; A_s is the cross-sectional area of CST; L is the apparent length of CST; C_1 is the concentration of acetone at CST exit/CSTR entrance; C_2 is the concentration of acetone at CST entrance/CSTR exit; m_R^{ads} is the mass of acetone adsorbed in the CSTR; and k, K, V_c^{act} are as defined earlier.

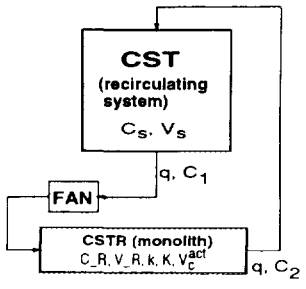

FIG. 9. CST/CSTR system configuration.

If we assume a well mixed recycle loop, with $A_sL = V_s$, then

$$V_s\frac{dC_s}{dt} = q(C_2 - C_1). \quad [19]$$

Equation [19] is the equation for a CST, with $C_s \equiv C_1$. A reactant species mass balance on the CSTR gives

$$q(C_1 - C_2) - \frac{kKC_RV_c^{act}}{1 + KC_R} = V_R\frac{dC_R}{dt} + \frac{dM_R^{ads}}{dt}. \quad [20]$$

Assumptions (CSTR):

- neglect mass transfer effects;
- reaction follows a simple LH rate form;
- well mixed system;
- isothermal.

Combining Eqs. [19] and [20] gives

$$-\frac{kKC_RV_c^{act}}{1 + KC_R} = \left(V_R\frac{dC_R}{dt} + V_s\frac{dC_s}{dt}\right) + \frac{dM_R^{ads}}{dt}, \quad [21]$$

with

$$V_s + V_R = V_g. \quad [22]$$

Combining terms,

$$V_g\frac{dC_g}{dt} = V_R\frac{dC_R}{dt} + V_s\frac{dC_s}{dt}. \quad [23]$$

Combining Eqs. [21] and [23] gives a single equation describing the destruction of a contaminant in the overall system (CST and CSTR):

$$-\frac{kKC_R V_c^{act}}{1+KC_R} = V_g\frac{dC_g}{dt} + \frac{dM_R^{ads}}{dt}. \quad [24]$$

Equation [24] has no remaining unknown parameters; once solved, it will be a completely predictive model of the experimental system.

Substituting Eq. [3] (a Langmuir adsorption isotherm for acetone on the coated monolith) into Eq. [24] (with $M_R^{ads} \equiv M_A^{ads}$),

$$-\frac{kKC_R V_c^{act}}{1+KC_R} = V_g\frac{dC_g}{dt} + \frac{d}{dt}\left(\frac{\mu_A K_A C_R}{1+k_A C_R + K_w C_w}\right). \quad [25]$$

The assumption is made that the conversion per pass in the system is very low, thus the gas-phase concentration throughout the system is nearly uniform ($(C_s \approx C_R) \equiv C_g$), and

$$-\frac{kKC_g V_c^{act}}{1+KC_g} = V_g\frac{dC_g}{dt} + \frac{d}{dt}\left(\frac{\mu_A K_A C_g}{1+K_A C_g + K_w C_w}\right). \quad [26]$$

Integrating Eq. [26] assuming a constant temperature (T) and gas-phase water concentration (C_w) yields the final predictive model equation, given by

$$kKV_c^{act}t = \left(V_g + \frac{\mu_A K_A}{1+K_w C_w}\right)\ln\left(\frac{C_g(0)}{C_g(t)}\right) + KV_g(C_g(0) - C_g(t)) - \left(\frac{\mu_A K_A}{1+K_w C_w}\right)\ln\left(\frac{1+K_A C_g(0)+K_w C_w}{1+K_A C_g(t)+K_w C_w}\right) - (\mu_A K(1+K_w C_w) - \mu_A K_A)\left(\frac{1}{1+K_A C_g(0)+K_w C_w} - \frac{1}{1+K_A C_g(t)+K_w C_w}\right). \quad [27]$$

The rate parameters are known from initial rate data, and the adsorption parameters from the isotherm determinations. Equation [27] should be predictive for all reaction time provided that no kinetically important intermediates or by-products appear. None were observed. To test this hypothesis, Eq. [27] was evaluated at the same conditions as the five experimental transient runs. Model and experiment are compared in Fig. 10. The model gives reasonable agreement for the concentration verses time data in all five runs over all degrees of conversion measured (up to 90%).

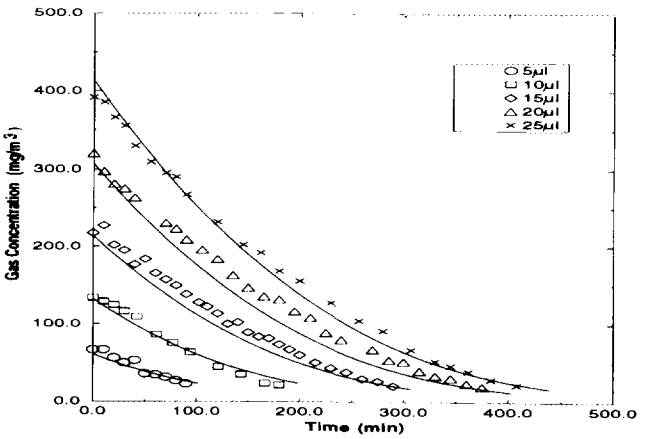

FIG. 10. Predictive model of the full transient system behavior for acetone.

4. DISCUSSION

4.1. Pseudo-First-Order Analysis

Suzuki *et al.* (Toyota R/D) studied photooxidation of trace odor compounds in air over TiO_2 in the first report of a photocatalytic monolith recirculating batch reactor (7). Acetaldehyde, isobutyric acid, toluene, methylmercaptan, hydrogen sulfide, and trimethylamine were individually converted, and analyzed as a pseudo-first-order process. Pseudo-first-order rate constants reported for several of the contaminants were very similar (Table 2). Each contaminant was run both with and without photocatalyst present to show the net effect of the presence of illuminated catalyst in the system.

Suzuki *et al.* (7) limited their kinetic analysis to a simple pseudo-first-order treatment. However, their plots of log (concentration) vs time showed a downward bend, imply-

TABLE 2

Previous Pseudo-First-Order Rate Constants (7)

Odor	Rate constant (min^{-1})
CH_3CHO	0.11
$(CH_3)_2CHCOOH$	0.0078
$CH_3C_6H_5$	0.059
CH_3SH	0.13
H_2S	0.13
$(CH_3)_3N$	0.16

ing that a Langmuir–Hinshelwood rate form might provide a better description of the results than the pseudo-first-order law assumed. They also reported some disappearance of the reactants in the absence of catalyst; in an air-tight system, this slow disappearance may be caused by homogeneous photolysis, by slow adsorption of reactant onto the ceramic monolith in their recirculating batch system, or both. The present study has shown that accounting for reversible adsorption of reacting species on the coated monolith leads to an accurate description of the batch recycle system behavior.

4.2. System Comparison

We want to compare acetone photooxidation results from two different systems (monolith reactor (present study) and steady-state flow reactor (4)). The two systems have two main differences that need to be accounted for to allow a useful comparison of the results. These differences are the water concentration and light intensity used for each system since the acetone photooxidation is expected to be dependent on these two factors.

Kinetic parameters for the photooxidation of acetone by a TiO_2 powder layer were previously determined (4) in a steady state flow photoreactor for a water concentration of 1000 ppm (1290 mg/m^3):

$$k = 7.75 \frac{\text{mg}}{\text{cm}^3\text{cat} - \text{min}} \quad [28]$$

and

$$K = 0.00644 \frac{\text{m}^3}{\text{mg}}. \quad [29]$$

The reaction rate constant (k) can be corrected to eliminate water influence, thus allowing a comparison between the previous steady-state system and present monolith transient system. The adjustment for water concentration is necessary since water inhibits acetone photooxidation according to the rate constant form [$k_0 = k(1 + K_{w_A} C_w^a)$], where $K_{w_A} = 9.6 \times 10^{-7}$ m^3/mg and $a = 1.674$ (4). The reaction rate constant and binding constant for the monolith system are given in Eqs. [14] and [15] for a water concentration of 11,067 mg/m^3. The modified reaction rate constants are:

monolith system,

$$k_0 = 2.66 \frac{\text{mg}}{\text{cm}^3\text{cat} - \text{min}}; \quad [30]$$

steady state system,

$$k_0 = 8.95 \frac{\text{mg}}{\text{cm}^3\text{cat} - \text{min}}. \quad [31]$$

These reaction rate constants are independent of water, but are still dependent on the intensity of light in the reactor. The previous steady-state system utilized an illumination source perpendicular to a bed of powder TiO_2, while the monolith reactor was illuminated parallel to the catalyst layer. Teichner and co-workers (1) found that 99+% of light adsorption occurred with a 4.5-μm film of TiO_2. Thus, for the steady-state system the catalyst bed has a constant illuminated catalyst thickness across the reactor cross section, while the illumination for the monolith system is more complex since the angle of incident light decreases toward the center of the monolith. This leads to an illuminated catalyst thickness that varies with location along the monolith. The active catalyst volume was calculated using a simple geometrical analysis of the maximum angle of incident light possible at each point in the monolith and then integrating the resulting catalyst thickness over the entire monolith length to calculate the maximum possible active catalyst volume (see the Appendix):

$$V_c^{\text{act}}(\text{maximum}) = 0.20\,\text{cm}^3. \quad [32]$$

If instead the assumption is made that the active catalyst thickness is a uniform 4.5 μm throughout the monolith the resulting active catalyst volume would be 1.61 cm^3. Thus, accounting for the decreasing illumination depth within the monolith leads to an active catalyst volume that is about a factor of 8 lower than that which a powder layer would provide with vertical illumination.

We modify the reaction rate constants further to account for the different illumination intensities of the two systems. Both systems utilized the same lamps, but these were located at different distances from the reactors. If we assume that light intensity decreases inversely with the square of distance from the lamp,

$$I_{\text{reactor}}(I_R) = \frac{P_{\text{lamp}}}{L^2}, \quad [33]$$

where I_R is the average intensity of light in the reactor (ein/(m^2 − min)); P_{lamp} is the emitted power of lamp (ein/min); and L is the distance from lamp to reactor (cm).

The lamps emitted power is $P_{\text{lamp}} = 1.33 \times 10^{-4}$ ein/min. For the steady-state system, where $L = 13$ cm,

$$I_R = 7.87 \times 10^{-3} \frac{\text{ein}}{\text{m}^2 - \text{min}}. \quad [34]$$

The monolith system with $L = 23.1$ cm, provides

$$I_R = 2.49 \times 10^{-3} \frac{\text{ein}}{\text{m}^2 - \text{min}}. \quad [35]$$

The new reaction rate constant (k_{new}) is expected to be independent of light intensity,

$$k_{new} = \frac{k_0}{I_R^{\alpha}}, \quad [36]$$

where α was determined to be 0.7 for the steady-state system by Peral and Ollis (4). We will assume this value for α is valid for the monolith system since the same Degussa P25 TiO_2 catalyst and lamp were used. Equation [36] gives:

steady state system,

$$k_{new} = 266 \left(\frac{mg}{cm^3 cat - min}\right) \Big/ \left(\frac{ein}{m^2 - sec}\right); \quad [37]$$

monolith system,

$$k_{new} = 177 \left(\frac{mg}{cm^3 cat - min}\right) \Big/ \left(\frac{ein}{m^2 - sec}\right). \quad [38]$$

The binding constants are:

steady state system,

$$K = 0.00644 \frac{m^3}{mg}; \quad [39]$$

monolith system,

$$K = 0.0107 \frac{m^3}{mg}. \quad [40]$$

Next, the initial reaction rates for the two systems are compared for an acetone gas phase concentration of 100 mg/m^3, a water concentration of 1000 mg/m^3 and a reactor light intensity (I_R) of 5.0×10^{-3} ein/(m^2 − min),

$$-r_A(0) = \frac{k_{new} K I_R^{0.7} C_g(0)}{(1 + KC_g(0))(1 + K_{w_A} C_w^a)}. \quad [41]$$

Thus, correcting for different intensity, humidity, and illumination depths gives similar reaction rate predictions from powder and monolith data:

steady state system,

$$-r_A(0) = 2.32 \frac{mg}{cm^2 cat - min}; \quad [42]$$

monolith system,

$$-r_A(0) = 2.03 \frac{mg}{cm^3 cat - min}. \quad [43]$$

5. CONCLUSIONS

An acetone (70–400 mg/m^3) contaminated air stream was treated in a catalyst coated monolith photoreactor system utilizing near-UV illuminated TiO_2. Adsorption isotherms for water (modified BET isotherm) and acetone (Langmuir isotherm) were measured and incorporated into an initial rate kinetic analysis. The resultant rate equation is shown to provide a predictive model for the full transient behavior of the monolith system at all acetone concentrations and conversions used.

APPENDIX

Estimation of Maximum Active Catalyst Volume

Assumptions:

- Any incident light from outside of the radius R_L on the lamp does not enter the system.
- Each monolith channel is identical to the channel located on the centerline with the lamp.

The dimensions and nomenclature used for the calculation are (refer to Fig. 11), R_L = 3.81 cm (1.5 in.), L_{Lamp} = 19.3 cm, $L_{monolith}$ = 15.24 cm, D = 0.424 cm, x = 4.5 μm, beta = β, and delta = δ.

The calculation can be broken into two sections: (i) the entrance region of the monolith where none of the incident light is shadowed by the monolith channel wall ($z \leq 2.27$ cm) and (ii) the interior monolith section that has some shadowing of the incident light ($z > 2.27$ cm).

For any point on the monolith,

$$\delta = x \sin(\beta). \quad [44]$$

For $z \leq 2.27$ cm,

$$\beta = \arctan\left(\frac{R_L + D/2}{L_{Lamp} + z}\right) \quad [45]$$

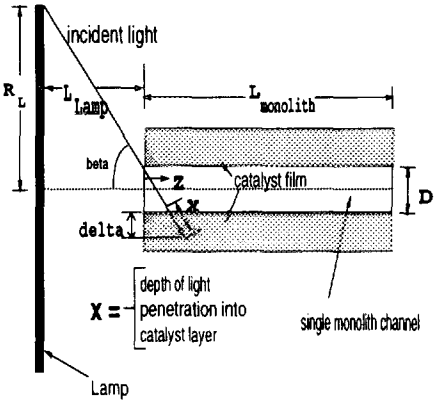

FIG. 11. Lamp and monolith geometries that were used to estimate the maximum active catalyst volume.

$$\delta = x \sin\left(\arctan\left(\frac{R_L + D/2}{L_{Lamp} + z}\right)\right). \quad [46]$$

For $z > 2.27$ cm,

$$\beta = \arctan\left(\frac{D}{z}\right), \quad [47]$$

$$\delta = x \sin\left(\arctan\left(\frac{D}{z}\right)\right). \quad [48]$$

The maximum active catalyst volume is,

$$V_c^{act} = 2\int_0^{L_{monolith/2}} NP_{channel}\delta\, dz, \quad [49]$$

where N is the number of monolith channels (138) and $P_{channel}$ = cross section perimeter of a single monolith channel (1.696 cm).

Substituting for δ,

$$V_c^{act} = 2NP_{channel}x\left(\int_0^{2.27} \sin\left(\arctan\left(\frac{R_L + D/2}{L_{Lamp} + z}\right)\right) dz + \int_{2.27}^{L_{monolith/2}} \sin\left(\arctan\left(\frac{D}{z}\right)\right) dz\right). \quad [50]$$

The resultant maximum active catalyst volume is

$$V_c^{act} = 0.20\ \text{cm}^3. \quad [51]$$

ACKNOWLEDGMENTS

This work was supported by NASA (NAG 2-684) and by a Hoechst-Celanese Kenan Fellowship for Environmental Science and Technology. We acknowledge helpful comments from NASA's Advanced Life Support Technology Program, Office of Aeronautics, Exploration and Technology.

REFERENCES

1. Formenti, M., Juillet, F., Meriaudeau, P., and Teichner, S. J., *Chem. Tech.* **1,** 680 (1971).
2. Teichner, S. J., and Formenti, M., *in* "Photoelectrochemistry, Photocatalysis and Photoreactors," p. 457. Reidel, Dordrecht, 1985.
3. Ibusuki, T., and Takeuchi, K., *Atmos. Environ.* **20,** 1711 (1986).
4. Peral, J., and Ollis, D. F., *J. Catal.* **136,** 554 (1992).
5. Dibble, L. A., and Raupp, G. B., *Catal. Lett.* **4,** 345 (1990).
6. Dibble, L. A., and Raupp, G. B., *Environ. Sci. Technol.* **26,** 492 (1992).
7. Suzuki, K., Satoh, S., and Yoshida, T., *Oenki Kagaku* **59,** 521 (1991).
8. Nimlos, M. R., Jacoby, W. A., Blake, D. M., and Milne, T. A., *Environ. Sci. Technol.* **27,** 732 (1993).
9. Raupp, G. B., Junio, C. T., *Appl. Surf. Sci.*, in press.
10. Irandoust, S., and Andersson, B., *Catal. Rev.-Sci. Eng.* **30,** 341 (1988).
11. Votruba, J., Mikus, O., Hlavacek, V., and Skrivanek, J., *Chem. Eng. Sci.* **29,** 2128 (1974).
12. Heck, R. H., Wei, J., and Katzer, J. R., *in* "Chemical Reaction Engineering 2," p. 34, (R. F. Gould, Ed.) American Chemical Society, 1974.
13. Plog, B. A. (Ed.), "Fundamentals of Industrial Hygiene," p. 272. National Safety Council, Chicago, 1988.
14. Adamson, A. W., "Physical Chemistry of Surfaces," Wiley, New York, 1976.